Nonlinear Barotropic Instability of Upper-Tropospheric Tropical Easterly Jet on the Sphere

S. K. MISHRA

Indian Institute of Tropical Meteorology, Pune, India

(Manuscript received 10 February 1992, in final form 11 August 1992)

ABSTRACT

The nonlinear evolution of perturbation superimposed on the barotropic, unstable observed mean easterly jet at 100 hPa is studied over the sphere. The nondivergent barotropic nonlinear global spectral model with rhomboidal truncation at zonal wavenumber 21 is integrated for 120 days for initial random and linear unstable perturbations. The model includes a Rayleigh friction and restoring mechanism for zonal wind to its initial distribution. Time variations of eddy and zonal kinetic energy, zonal–wave and wave–wave interactions, and eddy and zonal kinetic energy dissipations are examined. The growth of perturbation begins with exponential increase in its kinetic energy for a short period, followed by a linear increase. The perturbations undergo oscillations before approaching a steady state. During the initial exponential phase, the nonlinear interactions further destabilize the jet, and this effect is more pronounced for the random initial perturbation. It is found that oscillations in kinetic energy are due to the time lag between energy source (zonal–wave interaction) and sink (frictional dissipation).

It is noticed that the random initial perturbation is more efficient than the linear unstable modes in reaching the steady state. Nonlinear interactions shift the preferred wave towards the lower wavenumber 6. Wave 6 accounts for more than 98% of eddy kinetic energy of steady state. The role of wave–wave interaction is secondary to zonal–wave interaction.

Steady-state wave 6 has an inviscid growth rate of 0.104×10^{-5} s^{-1}, a phase speed of $-20.9°$ day^{-1}, and a meridional scale comparable to the half-width of the easterly jet. The zonal scale of the wave is close to the Rossby radius of deformation. The maximum meridional velocity associated with the wave is 3.8 m s^{-1}. Nonlinear interactions modify the jet to a more asymmetric distribution, which induces a southward shift in the wave-amplitude maximum location. Strong correlation between latitude of maxima for wave amplitude and meridional gradient of basic-state potential vorticity is noticed. A close agreement is seen between observation and nonlinear preferred wave 6.

The kinetic energy cycle for steady-state wave 6 on the sphere and in the latitude belt 10°S–40°N is computed and discussed. The kinetic energy of wave 6 in the latitude belt agrees well with the observed value.

1. Introduction

Linear barotropic (Mishra et al. 1981), baroclinic (Mishra and Salvekar 1980), and barotropic–baroclinic (Shukla 1977; Mishra and Tandon 1983) instability studies of observed mean monsoon easterly jet using dry, quasigeostrophic, beta-plane models have provided the broad physical basis to understand the formation and growth mechanism of observed synoptic-scale disturbances (zonal wavenumber 6–8) in the vicinity of an upper-tropospheric tropical easterly jet. Mishra (1987) has performed the barotropic instability of observed mean easterly jet over the sphere and obtained a Rossby wave of wavenumber 7 as the most preferred wave. Schoeberl and Lindzen (1984) have studied the influence of wave–zonal mean interaction in the evolution of unstable barotropic modes of a point easterly jet on a beta plane. It can be seen from their results that the most unstable linear mode (wavenumber 9) attains the largest enstrophy in the quasi-linear experiments, and they also concluded that the role of wave–wave interaction in the evolution process is insignificant. Mishra (1990) has studied the effect of zonal–wave and wave–wave interaction for the barotropic unstable observed easterly jet by using a global spectral model and choosing an initial state as a single unstable wave superimposed on the zonal jet. He found that the wave–zonal flow interaction leads to an oscillation in wave kinetic energy and that oscillation amplitude is maximum for initial wavenumber 7, while wavenumber 6 is the most unstable linear wave.

Kwon and Mak (1988) extensively studied the nonlinear barotropic instability of an easterly Bickley jet in a forced, dissipative, beta-plane model. They have shown that the equilibrium state may be either a steady-wave state, a vacillation cycle, or a chaos depending upon the values of nondimensional damping and forcing parameters. Further, it has been pointed out that

Corresponding author address: Dr. S. K. Mishra, National Centre for Medium-Range Weather Forecasts, Lodi Road, New Delhi, 110003.

systematic change in the scale selection can take place due to nonlinear dynamics.

It is known that the maintenance and strengthening of upper-tropospheric zonal easterlies in the tropics during the summer monsoon is due to the removal of westerly momentum by stationary long waves 1 and 2 (Krishnamurti 1971). Further, mean ascending motions over the warm land areas of Asia and descending motions over the relatively colder tropical ocean generate the eddy kinetic energy on the long waves (Krishnamurti et al. 1973). This will also lead to the maintenance of easterlies over the monsoon region. Hence, in a barotropic instability study of an easterly jet, inclusion of the restoring process will bring the results closer to reality.

In this paper an attempt is made to study the nonlinear barotropic instability of an observed mean tropical easterly jet in the presence of restoring force and dissipation on the sphere.

2. Model and system of equations

a. *A forced dissipative nonlinear barotropic model on a sphere*

The horizontal nondivergent motions on the surface of a rotating sphere of radius a and angular velocity Ω, in the presence of dissipation and vorticity source for the zonal flow, are governed by the following nondivergent barotropic vorticity equation:

$$q_t + \frac{(U\zeta)_\lambda}{a(1-\mu^2)} + \frac{(V\zeta)_\mu}{a} = -\alpha(\zeta - \bar{\zeta}_o), \quad (1a)$$

where

$$\mu = \sin\phi, \quad (1b)$$

$$q = \nabla^2\psi + 2\Omega\mu - R_e^{-2}\psi, \quad (1c)$$

$$\zeta = \nabla^2\psi, \quad (1d)$$

$$\bar{\zeta}_o = \nabla^2\bar{\psi}_o, \quad (1e)$$

$$U = -\cos\phi\ \frac{\psi_\phi}{a}, \quad (1f)$$

$$V = \frac{\psi_\lambda}{a}, \quad (1g)$$

$$R_e = \left(\frac{a^2 g^* H}{4\Omega^2}\right)^{1/2}. \quad (1h)$$

In the above equation, q is the potential vorticity; the overbar and o denote the zonal average and value at $t = 0$, respectively; ζ is the relative vorticity; ψ is the streamfunction; ϕ and λ are the latitude and longitude, respectively; R_e is the equatorial Rossby radius of deformation; g^* is the reduced gravity; α is the Rayleigh friction coefficient; and H is the constant thickness of the layer. Here frictional decay and restoring (relaxation) time scales are assumed to be equal to α^{-1}.

The term on the right-hand side of (1a) represents a simple and crude parameterized form of the physical and dynamical processes in the atmosphere that are responsible for restoring the zonal flow to its climatological mean value. The tendency to restore the zonal vorticity to its initial distribution is due to the imbalance between two opposite physical processes: the time invariant constant vorticity source term $\alpha\bar{\zeta}_o$ and the time-varying frictional dissipation term $\alpha\zeta$. At a latitude where zonal vorticity attains a value of less (more) than its initial value, the generation of vorticity by the source term is more (less) than the dissipation of vorticity by the frictional term. The term $-R_e^{-2}\psi_t$ in (1a) denotes the effect of divergence and vertical density stratification within the framework of a nondivergent barotropic model. Mishra (1981) has computed the values of g^* and H for the upper-tropospheric disturbances along the easterly jet as 0.786 m s^{-2} and 9 km, respectively, by considering a three-layer system of homogeneous, incompressible, nonviscous, and nonmixing barotropic fluid. The equatorial Rossby radius of deformation R_e is obtained as 1900 km.

b. *Numerical method*

The spectral method is used to obtain the numerical solution of (1a). The streamfunction is expanded as a spherical harmonic series using rhomboidal truncation at zonal wavenumber M:

$$\psi(\lambda, \phi, t) = \sum_{m=0}^{M} \sum_{n=m}^{m+M} (\psi_{1,n}^m \cos m\lambda + \psi_{2,n}^m \sin m\lambda) P_n^m(\mu), \quad (2)$$

where $P_n^m(\mu)$ is the associated Legendre function normalized to unity over the sphere; m and n are the zonal and two-dimensional wavenumbers, respectively; and $\psi_{1,n}^m$ and $\psi_{2,n}^m$ are spectral (spherical harmonic) coefficients. The spectral equations are obtained by substituting (2) in (1a) and using a full transform method for evaluating the nonlinear terms. The Euler backward and leapfrog time-differencing schemes are used for the first and subsequent time steps, respectively. The time-differencing scheme is backward with respect to the frictional term. The three-point recursive time filter of Robert (1966) is used with the filter parameter value of 0.01.

c. *Kinetic energy equation in wavenumber domain*

To diagnose the nonlinear evolution of unstable wave and to understand the role of wave–zonal flow and wave–wave interactions, the kinetic energy equation in zonal wavenumber domain is obtained. The global-average kinetic energy (AK) can be expressed as

$$\mathrm{AK} = \sum_{m=0}^{M} \mathrm{AK}(m), \quad (3a)$$

where $AK(m)$ denotes the global-average kinetic energy of the zonal wave m and can be written in terms of the global-average kinetic energy of the (m, n) mode $AK(n, m)$ as

$$AK(m) = \sum_{n=m}^{m+M} AK(n, m)$$

$$= \sum_{n=m}^{m+M} n(n+1)(\psi^m_{1,n}\psi^m_{1,n} + \psi^m_{2,n}\psi^m_{2,n})\frac{1}{8a^2} \quad (3b)$$

and

$$AK(o) = \sum_{n=1}^{M} AK(n, o)$$

$$= \sum_{n=1}^{M} n(n+1)\psi^o_{1,n}\psi^o_{1,n}\left(\frac{1}{4a^2}\right). \quad (3c)$$

The kinetic energy equation in wavenumber domain is obtained by differentiating (3b) and (3c) with respect to t and then substituting for time derivative terms from the spectral version of (1a):

$$AK(m)_t = WW(m) + ZW(m) - AD(m) - (1/R_e^2)a^2 \sum_{n=m}^{m+M} AK(n, m)_t \frac{1}{n(n+1)}, \quad \text{for } m > 0 \quad (4a)$$

and

$$AK(o) = -\sum_{m=1}^{M} ZW(m) - AD(o) + AG(o) - (1/R_e^2)a^2 \sum_{n=1}^{M} AK(n, o)_t \frac{1}{n(n+1)}, \quad (4b)$$

where

$$WW(m) + ZW(m) = \sum_{n=m}^{m+M} \frac{(\psi^m_{1,n}J^m_{1,n} + \psi^m_{2,n}J^m_{2,n})}{4}, \quad (4c)$$

$$-\sum_{m=1}^{M} ZW(m) = \sum_{n=1}^{M} \frac{\psi^o_{1,n}J^o_{1,n}}{2}, \quad (4d)$$

$$AD(m) = 2\alpha AK(m),$$

$$AD(o)(=AD_Z) = 2\alpha AK(o), \quad (4e)$$

$$AG(o)\,(=AG_Z) = \alpha n(n+1)\sum_{n=1}^{N} \psi^o_{1,n}\frac{(\psi^o_{1,n})_{t=0}}{a^2}.$$

Here $J^m_{1,n}$ and $J^m_{2,n}$ are the spectral representations of the advection term of the vorticity equation (1a); that is,

$$J = \frac{(U\zeta)_\lambda}{a(1-\mu^2)} + \frac{(V\zeta)_\mu}{a}.$$

The $WW(m)$ and $ZW(m)$ represent the gain of kinetic energy by wave m due to wave–wave and wave–zonal flow interactions, respectively; $AD(m)$ is the Rayleigh frictional dissipation for wave m; and $AG(o)$ is the generation of zonal kinetic energy. The wave–zonal flow interaction for wave m can be written as

$$ZW(m) = \int_{-1}^{1} \sum_{n=0}^{M} U^o_{1,n}P^o_n(U_{1,m}V_{1,m} + U_{2,m}V_{2,m})_\mu \times \left(\frac{4}{1-\mu^2}\right)d\mu, \quad (4f)$$

where $(U_{1,m}V_{1,m} + U_{2,m}V_{2,m})/2$ is the zonal-averaged meridional transport of zonal momentum at a latitude due to wave m. The integral in (4f) is evaluated by using the Gaussian quadrature method. The net gain of KE by wave m due to wave–wave interaction is obtained by subtracting wave–zonal flow interaction as computed from (4f) from the nonlinear wave interaction as computed from (4c).

The global area-averaged eddy (AK_E) and zonal (AK_Z) kinetic energy are given by

$$AK_E = \sum_{m=1}^{M} AK(m) \quad \text{and} \quad AK_Z = AK(o).$$

d. Zonally averaged kinetic energy equation

First, the zonally averaged wave kinetic energy K_E and zonal kinetic energy K_Z equations at a latitude are obtained from the linear viscous barotropic vorticity equation for perturbation and equation for zonal average vorticity. Then the resulting equations are averaged in the interval (μ_1, μ_2). It may be relevant to point out that quadratic (nonlinear) terms in the perturbation are neglected during the linearization process. Further, the nonlinear terms represent wave–wave interaction. Thus, wave–wave interaction from the energy equation has been neglected:

$$(K_E)_t = C(K_Z, K_E) - D_E - (1/R_e^2)\left\langle\left(\frac{\overline{\psi'^2}}{2}\right)_t\right\rangle + \text{boundary flux terms}, \quad (5a)$$

$$(K_Z)_t = -C(K_Z, K_E) - D_Z + GK_Z - (1/R_e^2)\left\langle\left(\frac{\overline{\psi}^2}{2}\right)_t\right\rangle + \text{boundary flux terms}, \quad (5b)$$

where

$$\langle (\ ) \rangle = (\mu_2 - \mu_1)^{-1} \int_{\mu_1}^{\mu_2} (\ ) d\mu,$$

$$K_E = \left\langle \frac{(\overline{U'^2} + \overline{V'^2})(1-\mu^2)^{-1}}{2} \right\rangle, \quad (5c)$$

$$K_Z = \left\langle \frac{\bar{U}^2(1-\mu^2)^{-1}}{2} \right\rangle, \quad (5d)$$

$$C(K_Z, K_E) = \langle \bar{U}(\overline{U'V'})\mu[a(1-\mu^2)]^{-1} \rangle, \quad (5e)$$

$$GK_Z = \alpha \langle \overline{UU}_o(1-\mu^2)^{-1} \rangle, \quad (5f)$$

$$D_E = 2\alpha K_E, \quad (5g)$$

$$D_Z = 2\alpha K_Z. \quad (5h)$$

Here the last terms on the right-hand side of (5a) and (5b) are a form of the eddy and zonal potential energy associated with the divergence, respectively; K_E and K_Z are the zonally averaged eddy and zonal kinetic energy in the latitude interval (μ_1, μ_2), respectively; $C(K_Z, K_E)$ denotes the barotropic energy transfer from zonal flow to the eddy; D_E and D_Z are the frictional dissipation of K_E and K_Z, respectively; and GK_Z is the generation of K_Z due to the forcing.

3. Initial state and relaxation parameter

The initial state chosen for numerical experiments is a small wave perturbation superimposed on basic zonal flow.

a. Basic zonal flow

The basic flow chosen for this study is the climatological mean monsoon (June–August) zonal wind at 100 hPa. The meridional profile of zonal wind is obtained by averaging mean zonal wind over the longitudes 55°–105°E. The $\bar{U}$ $(=\bar{u}\cos\phi)$ profile is fitted by a Legendre series truncated at latitudinal wavenumber $N = 21$. The $\bar{U}$ profile shows the maximum easterly of 27.5 m s^{-1} located at 14°N (Fig. 1). It may be relevant to state that the easterly jet satisfies the necessary condition for barotropic instability, whereas the midlatitude westerly jets do not satisfy the necessary condition.

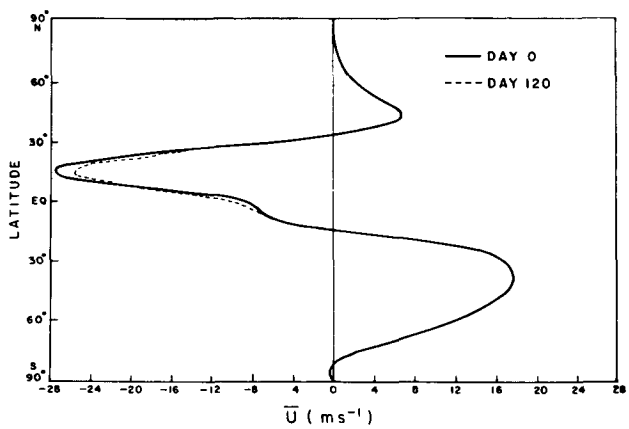

FIG. 1. Meridional profiles of latitudinal weighted zonal wind $\bar{U}$ $(=\bar{u}\cos\phi)$ (m s^{-1}) at initial time (solid) and at day 120 (dash) for the LIP case.

b. Perturbation

Two sets of numerical experiments are performed in this study. In one set of experiments, the initial wave perturbation is chosen as the random white noise having uniform kinetic energy spectrum. This experiment in short is denoted by RIP. In the second set of experiments, the initial perturbation is prescribed as a superimposition of linear unstable modes for wavenumbers 2–10 as obtained earlier by Mishra (1987) from the linear instability study. The unstable modes have the same kinetic energy. This experiment is designated as LIP.

c. Relaxation time

It is well established that the mean climatological features of the mean monsoon circulation in the upper troposphere—the easterly jet of south Asia is one of the important features—are described adequately by the combined field of zonal wavenumbers 0, 1, and 2. Further, the zonal wavenumbers 1 and 2 carry about 95% of variance of the stationary monsoon wind.

It can therefore be said that the quasi-stationary monsoon circulation is in a low-wavenumber mode. The strengthening and restoring of the easterly jet to its mean distribution, against the frictional dissipation and losses due to transfer of kinetic energy to the transient disturbances, is achieved by the conversion of stationary eddy available potential energy to the stationary eddy kinetic energy on planetary scales and conversion of zonal available potential energy to zonal kinetic energy. We have computed recently, stationary rotational zonal and eddy kinetic energy in zonal waves 1–4 and rotational–divergent wind interaction in the latitude belt 10°S–30°N and in the layer (300–100 hPa) for July 1979. Stationary eddy kinetic energy in waves 1–4, plus stationary zonal kinetic energy as computed by them, has a value of 40 J kg^{-1}; the sum of conversions from divergent to rotational kinetic energy for planetary-scale eddy and zonal flow is 10.5 W m^{-2}.

The e-folding time for the growth of rotational wind obtained from the value of energy and conversion is 8.8 days. This is a measure of relaxation time α^{-1}. A value of 10 days has been fixed for α^{-1} in the study.

4. Results

The value of rhomboidal truncation M is chosen as 21 keeping in view that the most unstable linear mode is wavenumber 7 (Mishra 1987). The time step Δt is chosen as 1 h. The model is integrated for 120 days in

all experiments reported here. The ratio of global area-averaged wave kinetic energy to the zonal kinetic energy at the initial time is fixed at 10^{-4} based on the quasi-linear numerical experiments performed by Mishra (1990), wherein it was shown that the results of wave–zonal flow interaction experiments are rather insensitive for the initial ratio values less than 10^{-4}.

a. Time variation of kinetic energy

Time variations of global-averaged eddy (AK_E) and zonal kinetic energy (AK_Z) for both numerical experiments are presented in Fig. 2. In the RIP case, the regular increase in AK_E takes place beyond day 28, before that the initial perturbation undergoes adjustments without a significant change in its kinetic energy. In contrast to this, the regular increase in AK_E is seen from the very beginning for the LIP case. In this case up to day 16, AK_E increases exponentially and thereafter the increase is linear in time. The exponential growth of AK_E is not noticed in the RIP case. After attaining the maximum value, AK_E shows an oscillatory behavior with decreasing amplitude and finally approaches a steady-state value. The two steady-state values are very close to each other and they differ by an amount less than 2.5% of their final values. The period of oscillation is about 24 days. It may be mentioned that for the same easterly jet, in absence of restoring mechanism and friction, in the single wave–zonal flow interaction experiment, an oscillation with a period of 35 days was also found (Mishra 1990). The

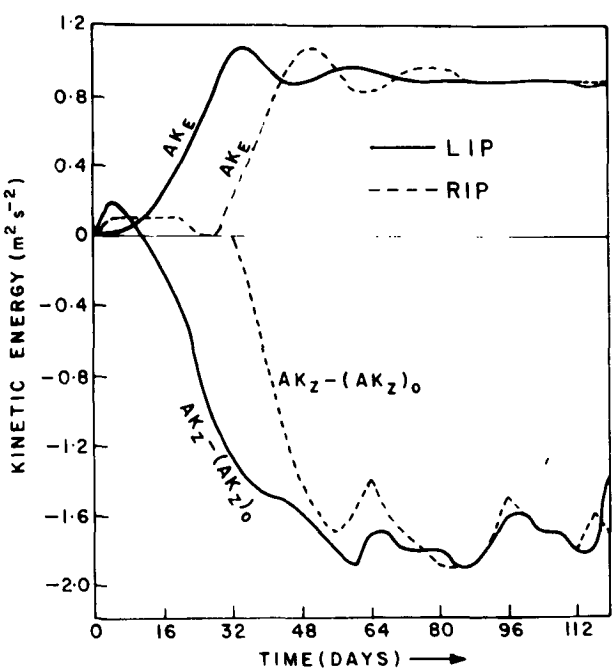

FIG. 2. Global-averaged eddy kinetic energy AK_E ($m^2\ s^{-2}$) and deviation of zonal kinetic energy ($m^2\ s^{-2}$) from its initial value [$AK_Z - (AK_Z)_o$] as a function of time for the RIP (dash) and LIP (solid) experiments.

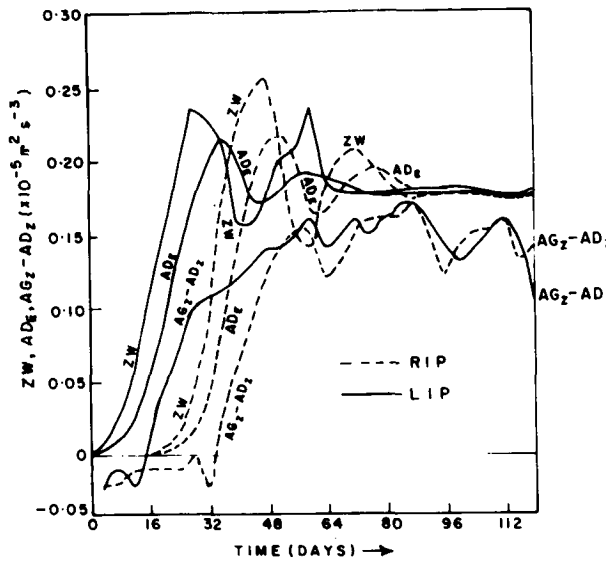

FIG. 3. Deviation of global-averaged zonal kinetic energy generation AG_z from zonal kinetic energy dissipation AD_z, eddy kinetic energy dissipation AD_E, and total zonal–wave interaction ZW as a function of time. Dashed and solid curves are for random (RIP) and linear unstable (LIP) initial perturbations, respectively. Units are 10^{-5} $m^2\ s^{-3}$.

observational study of Chen and Yen (1991) has shown that the tropical easterly jet possesses a distinctive intraseasonal 30–60-day oscillation in the latitude belt 5°N–10°S, which is to the south of the jet core. Further, in the wave–wave experiment with the single unstable wave for the initial state, oscillations with a variable period in the range of 25–35 days were also noticed. A comparison between the two time-variation curves has indicated that the two curves are nearly similar, except that the RIP curve lags behind the LIP curve by about 16 days, which nearly accounts for the time spent on initial adjustment by the random perturbation.

The oscillatory behavior of AK_E after initial adjustment and growth is due to opposite competitive processes of zonal–wave interaction and dissipation; while the former acts as a source, the latter acts as a sink for AK_E. During the growing phase, zonal–wave interaction is stronger than the dissipation process, while in the decay phase, dissipation is stronger than zonal–wave interaction, as concluded from Fig. 3. Throughout the period of integration, zonal–wave interaction does not change sign and it is positive. It may be relevant to note that in a earlier study, Mishra (1990) has also found oscillation in the quasi-linear evolution of a barotropic unstable wave where only the interaction between zonal flow and waves is allowed and is due to the reversal in the direction of zonal–wave interaction. It is important to note that the maximum value attained by the zonal–wave interaction in the RIP case is more than that achieved in the LIP case. This implies that due to presence of random initial perturbation,

the easterly jet is modified to a more unstable jet by wave–wave and zonal–wave interaction, compared to the case when initial perturbation was linear unstable modes.

It is observed that the maximum decrease in AK_Z from its initial value is more than the maximum gain in AK_E during the integration, even in the presence of a forcing mechanism for the zonal flow, which relaxes the zonal flow back to its initial profile. The root of this apparent contradiction lies in ignoring the amount of perturbation kinetic energy loss due to Rayleigh friction. For the initial random perturbation, the AK_Z curve exhibits more regular oscillation with larger amplitude compared to that for the initial state constructed from the linear unstable modes. The generation mechanism supplies energy to the zonal flow throughout the period of integration. Here AG_Z is in excess over the dissipation of AK_Z by friction except for a few days at the initial evolution of perturbation. It is understandable that the generation mechanism for AK_Z is responding to zonal–wave interaction, which is primarily responsible for the modification of zonal wind distribution. Hence, it is expected that $AG_Z - AD_Z$ curves will exhibit oscillation. What is difficult to understand is the oscillatory behavior of $AG_Z - AD_Z$ curves during the period when AK_E is tending towards the steady state as seen from Fig. 2.

It is noticed that up to day 16 of integration for initial linear unstable perturbation, wave 6 and 7 grow exponentially, as is the case with the corresponding linear waves (Fig. 4). The maximum growth rates of waves 6 and 7 are computed from their values of zonal–wave interaction (barotropic energy conversion), and not from their kinetic energy values, in order to exclude the damping effect of Rayleigh dissipation. It is necessitated because the growth rates of inviscid linear unstable waves are only available for comparison (Mishra 1987). The linear inviscid growth-rate spectrum for initial (day 0) zonal flow was obtained by using the initial value approach. The model integration was terminated when the relative error between two consecutive 6-h-averaged growth rates of the wave was less than a prespecified value (10^{-3}). The growth rate spectrum is presented in Fig. 5. Similarly, the growth rates for zonal wind profile at day 120 are computed. The growth-rate values that converged within 100 days of integration of the model are indicated by the cross symbol. This aspect will be further discussed in the next subsection. The maximum growth rates are 0.273 $\times 10^{-5}$ and 0.282 $\times 10^{-5}$ s^{-1} for waves 6 and 7, respectively, for the LIP case, as computed from barotropic energy conversions, whereas the corresponding values for the linear case are 0.25 $\times 10^{-5}$ and 0.27 $\times 10^{-5}$ s^{-1}, respectively (Fig. 5). These values for the RIP case are 0.289 $\times 10^{-5}$ and 0.287 $\times 10^{-5}$ s^{-1}, respectively. The nonlinear growth rate during the exponential growing phase is more than the linear wave for wavenumber 6 and 7, while for the other waves, opposite inequality is noticed. In the RIP case, the

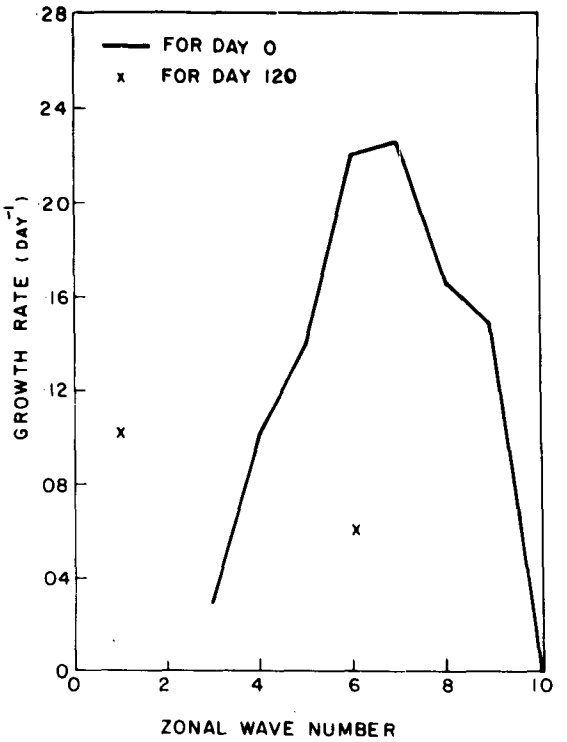

FIG. 5. Linear growth rate (day^{-1}) spectrum for the meridional profile of U at day 0 (−) and values obtained for day 120 are indicated by the symbol cross (×).

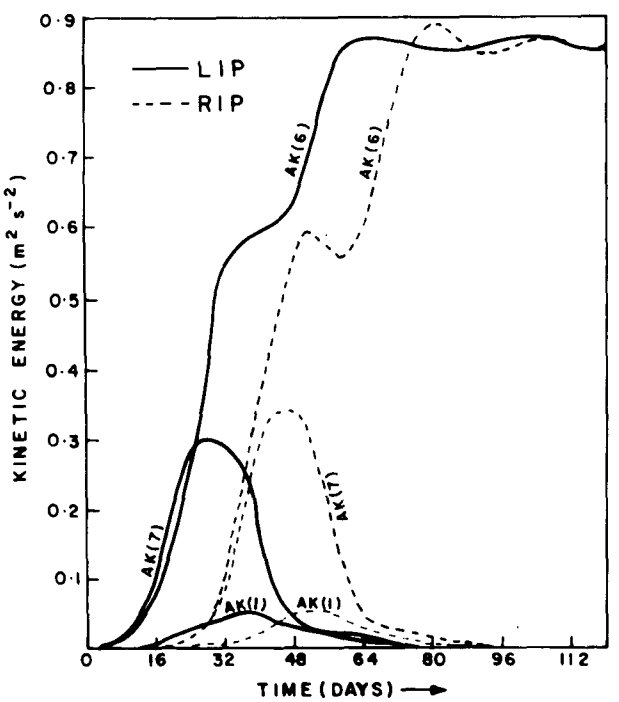

FIG. 4. Global-averaged kinetic energy (m^2 s^{-2}) as a function of time obtained from the RIP (dash) and LIP (solid) experiments for zonal wavenumber 1 [(AK(1)], 6[AK(6)], and 7[AK(7)].

maximum growth rates for wave 6 and 7 are even more than that for the LIP case. During day 16–24, the increase in kinetic energy for waves 6 and 7 is linear. Beyond day 24, it is wave 6, which dominates over all other waves to such an extent that it accounts for more than 98% of AK_E during steady state. It may be noted that wave 7 is most unstable in the linear case (Mishra 1987), but wave 6 is the preferred wave in a quasi-linear case (Mishra 1990). The above discussion leads to a physical picture that zonal-wave and wave-wave interactions optimize the tropical easterly jet to a barotropically more unstable state. This optimization is more effective in the case of initial random perturbation. Further, the nonlinear interactions also modify the easterly jet so that the unstable wave spectra is narrow, which is in contrast to a situation when interactions lead to a turbulent state where the eddies involved have a wide band of wavelengths.

An examination of zonal-wave interaction spectrum as a time series indicates that during the initial growth the values differ by a factor of 2 in the wave interval 3–9. With the passage of time, the zonal-wave interaction for waves other than wave 6 weaken, and they are 3–5 orders less than the value for wave 6. Thus, the very weak zonal-wave and wave-wave interactions in presence of dissipation lead to a single wave 6 domination in the steady state.

Wave 6 receives kinetic energy from zonal flow due to zonal-wave interaction throughout the integration, which is more than the loss due to frictional dissipation and wave-wave interaction (Fig. 6). For wave 6, the wave-wave interaction (Fig. 7) is one order smaller than the zonal-wave interaction and frictional dissipation, which are of the same order. The wave-wave (self) interaction for wave 6 generates subharmonics 12 and 18, whose kinetic energy is two orders smaller than wave 6 in the steady state. Further, the wave-

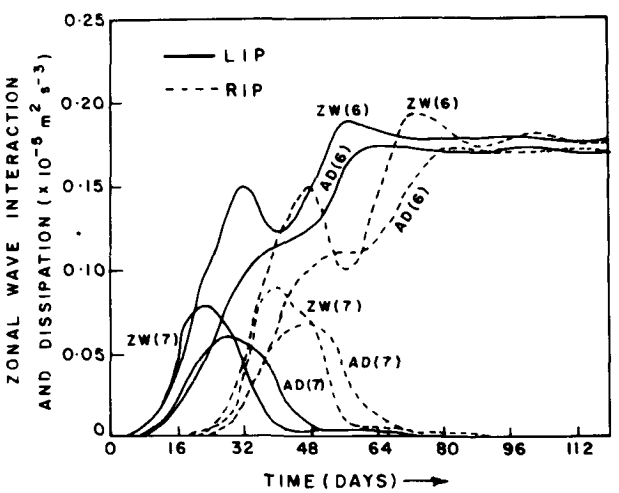

FIG. 6. Zonal-wave interaction (ZW) and dissipation of KE (AD) as a function of time for wavenumber 6 and 7. Dashed and solid curves are for initial random (RIP) and linear unstable (LIP) perturbations, respectively. Units are 10^{-5} m^2 s^{-3}.

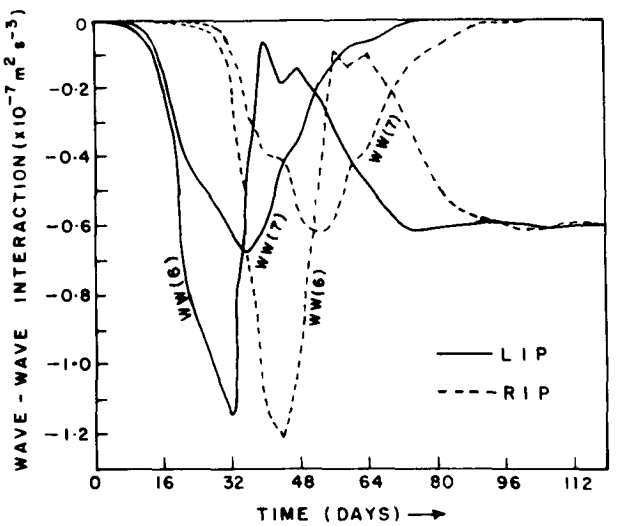

FIG. 7. Wave-wave interaction of KE (WW) as a function of time for wavenumber 6 and 7. Dashed and solid curves are for initial random (RIP) and linear unstable (LIP) perturbations, respectively. Units are 10^{-7} m^2 s^{-3}.

wave interaction between waves 6 and 7 is found to induce a very weak wave 1. It may be worth mentioning that the linear stability analysis of an easterly jet has shown that wave 1 is stable. A comparison between Figs. 6 and 7 for wave 6 indicates that when the excess of zonal wave interaction over the dissipation loss reaches a maximum (minimum) value, the loss due to wave-wave interaction is also maximum (minimum). Further, it is concluded by examining the time variation of zonal-wave interaction for wave 6 (Fig. 6) and AK_E (Fig. 2) that the oscillation exhibited by the latter is preceded by the oscillation in the former.

Wave 7 shows a single growth and decay cycle. An examination of zonal-wave interaction, dissipation rate, and wave-wave interaction for wave 7 indicated that during the growth phase, gain of kinetic energy by wave 7 is more than the combined loss due to frictional dissipation and wave-wave interaction, while in the decay phase, the opposite relationship between them is noticed. The role of wave-wave interaction in the evolution of wave 7 is found to be secondary.

b. Steady-state solution

The closeness of the numerical solution at day 120 to its steady-state solution is measured by the maximum departure of eddy kinetic energy during the period 100–120 days from its mean value in the same period, expressed as a percentage. For the RIP case, the maximum departure in eddy kinetic energy is about 0.8%, while for the LIP case, the value is about 1.1%. Kinetic energy and zonal-wave interaction spectra at day 120 are presented in Table 1. It is seen that wave 6 accounts for more than 98% of the eddy kinetic energy on day 120. Therefore, the results pertaining to wave 6 at day 120 are presented for the RIP case. The

TABLE 1. Zonal-wave interaction ZW (10^{-10} m^2 s^{-3}), kinetic energy AK (10^{-4} m^2 s^{-2}), and growth rate GR (day^{-1}) as a function of zonal wavenumber m.

m	1	2	3	4	5	6	7	8	9	10
AK	5.12	1.26	0.171	8.94	3.06	0.860×10^4	2.03	0.503	0.030	0.424
ZW	13.4	0.694	0.087	14.8	−0.595	0.180×10^5	2.97	−0.554	0.054	0.394
GR = ZW/(2AK)	0.113	0.024	0.022	0.071	−0.008	0.09	0.063	−0.047	0.077	0.040

zonal-wave interaction values for waves other than wave 6 are five to six orders less than the value for wave 6. It can be said that the zonal-wave interactions, except for wave 6, are comparable to the expected truncation error for a 32-bit computer system. Thus, these values are not accurate enough for computation of growth rates. The inviscid growth-rate spectra GR(m) at day 120 are computed from the zonal-wave energy transfer ZW(m) and kinetic energy AK(m) spectra at day 120 by using the formula GR(m) = ZW(m)[2AK(m)]$^{-1}$. The wave has a growth rate of 0.09 day^{-1}, as implied by the zonal-wave energy transfer. The linear growth rate value for wave 6 as obtained by the initial value approach is 0.06 day^{-1}. Wave 6 has a westward phase speed of 20.9° day^{-1}, which is close to the value of −20.7° day^{-1} for linear wave 6. In the inviscid sense, the wave is weakly unstable. In order to confirm this conclusion, the $\bar{q}_\mu/a$ profile at day 120 is examined and compared with the profile at day 0. The two profiles are presented in Fig. 8. It is seen from the figure that the easterly jet at day 120 is weakly unstable compared to the initial jet. This conclusion is based on the negative maximum value of the $\bar{q}_\mu/a$ profile at day 120, which is 0.18 $\times 10^{-11}$ m^{-1} s^{-1}, while the value is 1.2×10^{-11} m^{-1} s^{-1} for the initial profile. The maximum meridional velocity associated with the unstable wave is 3.8 m s^{-1}, which is very close to the observed value for transient

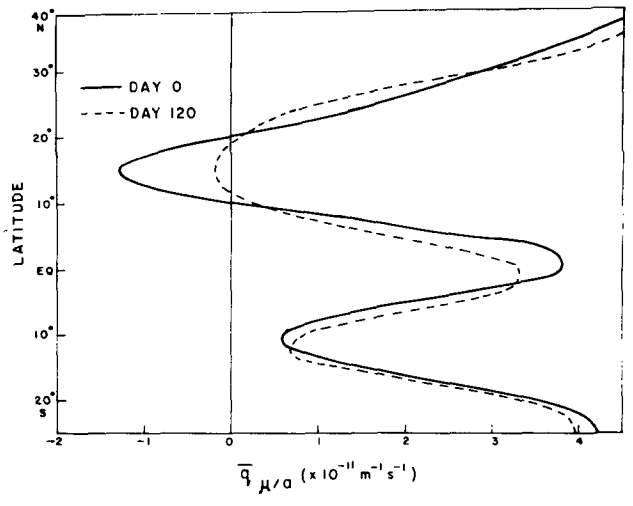

FIG. 8. Meridional profile of the meridional gradient of basic-state potential vorticity $\bar{q}_\mu/a$ (10^{-11} m^{-1} s^{-1}) at day 0 and 120 for the LIP case.

waves in the vicinity of the easterly jet, as computed by Krishnamurti (1971).

In order to compare the structure of steady-state wave 6 with the linear preferred wave 7, the streamfunction distribution in the latitude–longitude plane after normalization is presented in Fig. 9. The maximum value of streamfunction is normalized to 10. Except for the structure in all other computations, wave 6 is not normalized and, as obtained in the nonlinear model integration at day 120, is used. The wave has a maximum amplitude located close to the equator at 1°N. The location of amplitude maximum is to the south of the latitude of the linear wave primary amplitude maximum located at 3.5°N. It has been shown by Mishra (1981) using a linear nondivergent beta plane model that the asymmetry in the easterly jet around its center is responsible for the southward shift of the preferred wave amplitude maximum. He has also shown that antisymmetric components of the easterly jet explain only 8% of the total variance of the zonal wind, while the same antisymmetric components account for about 37.5% of variance in the asymmetric profile of the meridional gradient of basic-flow absolute vorticity. A comparison of easterly wind profiles at day 0 and 120 clearly indicates that in addition to a decrease in the easterly wind maximum, the easterly wind to the north decreases, while to the south it is increased at day 120 compared to that at day 0 (Fig. 1). The easterly jet at day 120 is more asymmetric than at day 0. Further, the $\bar{q}_\mu/a$ profiles exhibit more clearly the strengthening of antisymmetric components around the jet center for day 120 over the profile at day 0. Thus, it can be concluded that the southward shift of the wave-amplitude maximum of a nonlinear steady-state wave with respect to the linear wave is due to the increase in the asymmetric nature of the jet at day 120 over the jet used in the linear case (day 0). The correlation between the amplitude maximum and the positive maximum of $\bar{q}_\mu/a$ is more valid for the nonlinear case than the linear case.

The wave exhibits an eastward tilt with latitude that is mainly confined in the latitude belt 0°–20°N. The tilt is more pronounced around the jet center. The tilt implies a southward transport of easterly momentum to the south as well as to the north of the jet center (13.75°N). The computed angular momentum transport ($\overline{U'V'}$) profile is shown in Fig. 10a. To the south (north) of the jet center, the divergence (convergence) of westerly angular momentum or convergence (divergence) of easterly angular momentum ($\overline{U'V'}_\mu > 0$

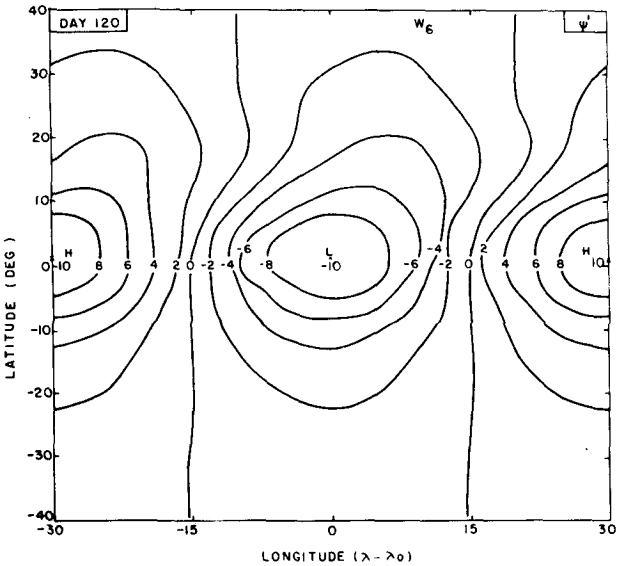

FIG. 9. Latitude–longitude distribution of normalized streamfunction of wave 6 at day 120 for the LIP case. The maximum value is normalized to 10. Here longitude is departure from the longitude of maximum value.

$[(\overline{U'V'})_\mu < 0)]$ is occurring, which is unfavorable (favorable) to growth of the wave. The divergence of easterly momentum in the north is stronger than the convergence of easterly momentum in the south. Hence, it is expected that there will be a net gain of kinetic energy for wave 6. The northward transport of easterly momentum associated with wave 6 is weakened and its latitude extent is reduced for the nonlinear case compared with the linear case. The ratio of maximum southward momentum transport to the maximum northward transport for the nonlinear case is 14.5, while for the linear case the ratio is about 2.5. Theoretically, the ratio has a value of 1 for a barotropic unstable wave in a midlatitude beta plane and for a symmetric jet. Southward easterly momentum transport attains a maximum value at 10°N, which coincides with the latitude of maximum transport for the linear preferred wave. The meridional profile of $\overline{U'V'}$ for the nonlinear case differs significantly from the linear case, but the shape of the $(\overline{U'V'})_\mu$ profiles in two cases is rather similar. This indicates that the meridional distribution of angular momentum transport for the nonlinear case can be approximately realized by adding a nearly constant southward flux of easterly angular momentum to the transport of the linear case. Further, the latitude of maximum transport coincides with the latitude of $\bar{q}_\mu = 0$, which implies the latitude of maximum $\bar{q}$.

It seems that the nonlinear evolution of wave 6 in terms of associated meridional transport of potential vorticity ($\overline{V'q'}$) has not deviated significantly from the linear theory for a symmetric jet, while the nonlinear and linear angular momentum flux distributions differ significantly from each other. Since the potential vorticity flux is just the convergence of the angular momentum flux, it is expected that the differences between linear and nonlinear flux distributions will be similar for potential vorticity and angular momentum. It has been stated above that while linear and nonlinear momentum flux distributions differ significantly, their convergences do not deviate significantly. The potential vorticity transport due to wave 6 is nearly antisymmetric around $\bar{q}$ maximum, with southward (northward) transport taking place to the south (north) of the maximum (Fig. 10b). The divergence of potential vorticity transport takes place around $\bar{q}$ maximum. Thus, the transfer of enstrophy from zonal flow to the perturbation takes place around $\bar{q}$ maximum.

It can be concluded easily from Fig. 9 that the wave amplitude decreases more slowly to the north than to the south of amplitude maximum. The latitudinal distance over which the wave amplitude decreases to one-half of its maximum value is found to be 11° in the south sector and 15° in the north sector. This north–south asymmetry in the variations of wave amplitude can be attributed to the variation in the refractive index with latitude. The steady-state wave 6 in presence of friction is very close to a neutral wave. Hence, the

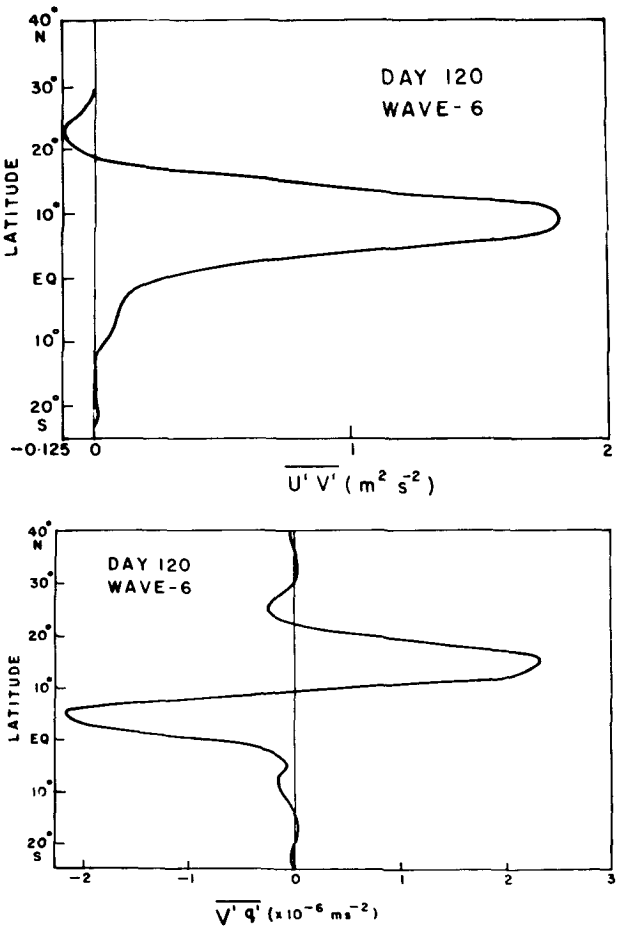

FIG. 10. Meridional profiles of (a) $\overline{U'V'}$ ($m^2 s^{-2}$) and (b) potential vorticity flux $\overline{q'V'}$ (10^{-6} m s^{-2}) due to wave 6 of the LIP case at day 120.

expression of the refractive index l^2 for meridional propagation of a neutral wave as derived by Mishra (1987) can be used:

$$l^2 = \frac{(1-\mu^2)[2\Omega - (\bar{U}_{\mu\mu}a^{-1}) + \omega_r a^2 R_e^{-2}]}{(\bar{\omega} - \omega_r) - m^2},$$

where $\bar{\omega} = \bar{u}/(a\cos\phi)$ is the angular velocity associated with the zonal wind and ω_r is the real part of complex angular velocity of a near neutral wave. The meridional propagation is possible if $l^2 > 0$, otherwise the propagation is not possible. A latitude where the condition $l = 0$ is satisfied is identified as a turning latitude. The turning latitude plays an important role in understanding the meridional propagation of a wave.

The computed refractive index profile for wave 6 at day 120 is presented in Fig. 11. The refractive index is computed on the grid interval of 2.5° latitude. It is clear that there exist two latitudinal zones, 6°S–9.5°N and 14°–20°N, that allow the meridional propagation of the wave. Thus, to the north of wave amplitude maximum, the wave propagation occurs in the wide latitude belt, compared with the south. The wave amplitude maximum is located in the latitude zone where the wave can propagate. The critical latitudes, where $\bar{\omega} = \omega_r$, are computed and the values are 13.2° and 18°N. In obtaining the critical latitudes, the linear interpolation in latitude is used between the 2.5° latitude grid. The largest maximum and lowest minimum of the refractive index profile are located at 17.5° and 12.5°N, respectively, which are close to the critical latitudes. The deviation of refractive-index extrema from the locations of critical latitudes may be partly due to low resolution of the latitude grid used for computation of the refractive index.

The meridional scale of the wave is measured as the half-width of streamfunction distribution, which is found to be 2850 km. The meridional scale of the easterly jet is 2600 km, as obtained from the meridional profile of $\bar{U}$ at day 120 (Fig. 1). Thus, the meridional scale of the wave is close to the meridional scale of the easterly jet but larger than the Rossby radius of deformation. Further, it can be said that the WKB approximation cannot be used to explain the meridional structure of the wave. In order to establish a relationship between the zonal scale of dominating wave 6 found in this study with the Rossby radius of deformation, the latitude where the wave amplitude reduces to one-half of its maximum value is considered. Such latitude worked out to be 14°N, where the easterly jet center is also located. Here $2k^{-1}$ is considered as the zonal scale of the wave of zonal wavenumber k because it estimates the average value of zonal derivatives instead of their maximum value (Mishra 1981). The zonal scale of wave 6 at latitude 14°N is 2060 km, which is close to the Rossby radius of deformation.

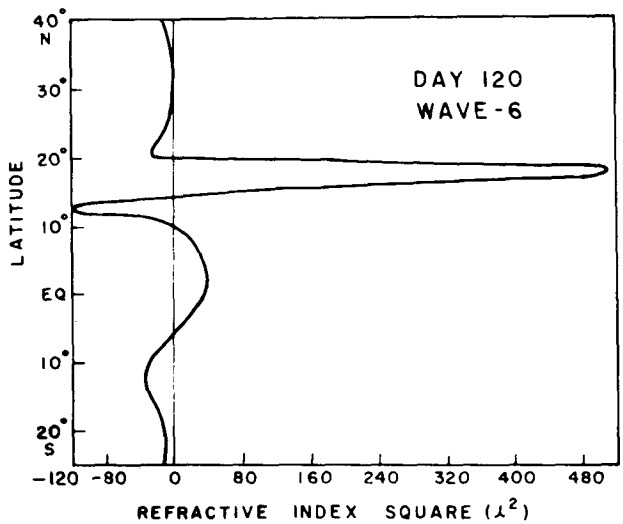

FIG. 11. Meridional profile of refractive index square l^2 for wavenumber 6 of the LIP case at day 120.

c. Steady-state kinetic energy cycle for wave 6

The global-averaged kinetic energy cycle for wave 6 at day 120 is illustrated in Fig. 12a. Wave 6 receives kinetic energy (AK_E) from zonal kinetic energy (AK_Z) due to zonal–wave interaction, which is adequate to maintain the wave against the loss of energy by friction and wave–wave interaction. The zonal flow is overcompensated by the generation mechanism against the losses due to dissipation and due to transfer of energy to wave 6. Zonal and wave 6 kinetic energy spectra as a function of pseudo latitudinal wavenumber $(n - m)$ are computed for day 120 but not presented. It is seen that the zonal kinetic energy spectrum has a peak at the wavenumber 3 and it accounts for about 52% of AK_Z. The pseudowavenumbers 2 and 3 together account more than 85% of AK_Z. Further, even and odd pseudolatitudinal wavenumber components account for 43.4% and 56.6% of AK_Z, respectively. The pseudowavenumber 0 contains more than 72% of AK_E, while wavenumbers 0 and 2 together account for more than 80% of AK_E. Further, even and odd pseudolatitudinal wavenumber components account for 94.04% and 5.6% of AK_E, respectively. Thus, the latitudinal distribution of wave 6 to a very good approximation is symmetric around the equator, while the basic zonal flow cannot be approximated as symmetric or antisymmetric around the equator. Hence, a hemispheric model cannot adequately describe the easterly jet dynamics.

The latitudinal profiles of barotropic energy conversion $C(K_Z, K_E)$, dissipation, and kinetic energy for wave 6 and a profile of zonal kinetic energy were computed and presented in Fig. 13. Wave 6 extracts kinetic energy from the zonal flow in the latitude belt 9°–22°N and attains a maximum at the easterly jet center. Wave 6 loses kinetic energy to the zonal flow in the belt 3°S–9°N. Thus, the source of energy for wave 6 is located around the jet center and is responsible for maintaining the wave not only locally but elsewhere through the energy fluxes. The zonal wind around the jet center is

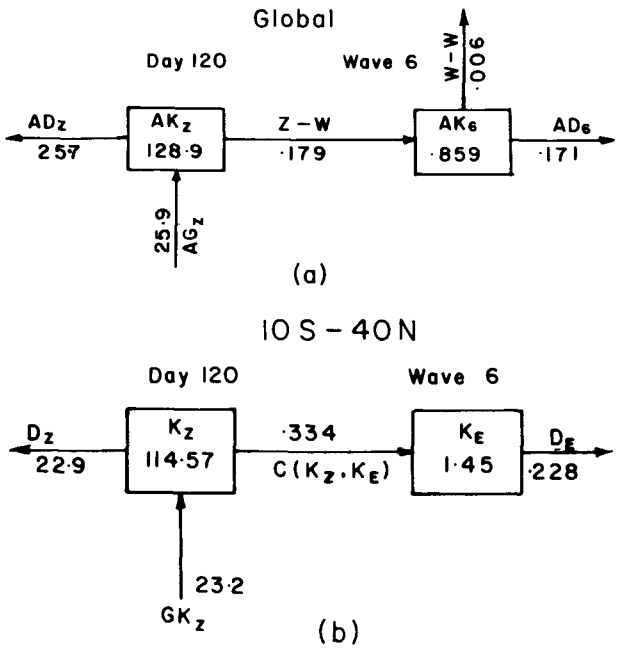

FIG. 12. Kinetic energy cycle for wave 6 of LIP at day 120 on (a) the globe and (b) the latitude belt 10°S–40°N. Units for kinetic energy are meters squared per second squared, and energy exchanges are in 10^{-5} m^2 s^{-3}.

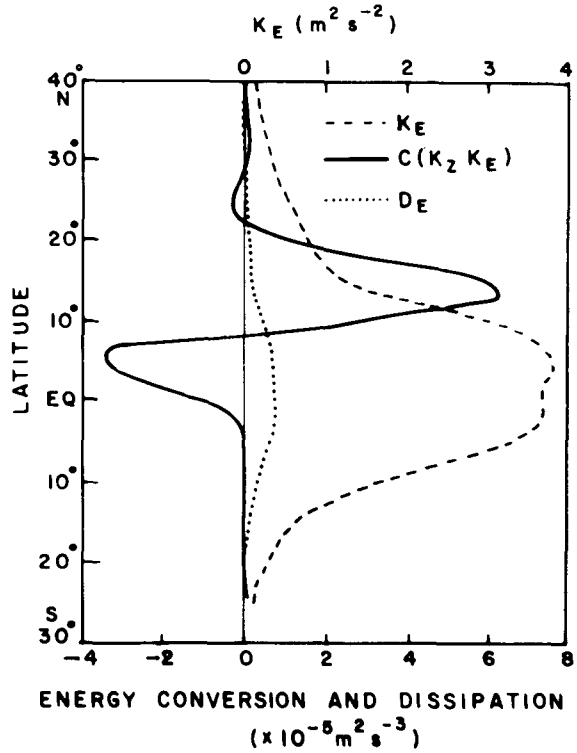

FIG. 13. Meridional profiles of barotropic energy conversion $C(K_Z, K_E)$, dissipation D_Z, and eddy kinetic energy K_E for wave 6 of the LIP case at day 120. Units for kinetic energy are square meters per second squared and energy transfers are in 10^{-5} m^2 s^{-3}.

maintained by the generation process. Not only GK_Z but also $GK_Z - D_Z$ attain the maximum value close to the jet center (Fig. 14). The average energy cycle in the latitude belt 10°S–40°N is obtained since wave 6 is essentially confined in this latitude belt and is shown in Fig. 12b. Wave 6 is receiving more kinetic energy due to the conversion than the loss due to friction. Wave 6 may remain in steady state in the region, provided the excess energy is transported away from the region through the boundary terms. The averaged observed transient kinetic energy of wave 6 in the latitude belt 10°S–30°N is 1.6 m^2 s^{-2}, which is in better agreement with the average value 1.45 m^2 s^{-2} obtained in this study using the large latitude belt than that used in the observational study.

5. Conclusions and discussion

It was not intended in this study to simulate or explain the life cycle of disturbances observed in the vicinity of an upper-tropospheric tropical easterly jet. It is known that both barotropic and baroclinic dynamics play an equally important role in the development of disturbances (Mishra and Tandon 1983), which is not included in the study. Our limited objective was to bring out the role of barotropic nonlinear process in the scale selection and development of eddies along the unstable easterly jet in the presence of Rayleigh friction and forcing to relax the zonal wind to its initial distribution on the rotating spherical earth. The observations indicate that the easterly jet exhibits an increasing trend along with fluctuations with the progress of monsoon over the Indian region. The increasing trend of the easterly jet is neglected in the study.

It has been shown that the random initial perturbation is more efficient in reaching the steady state than the initial state obtained by superimposition of

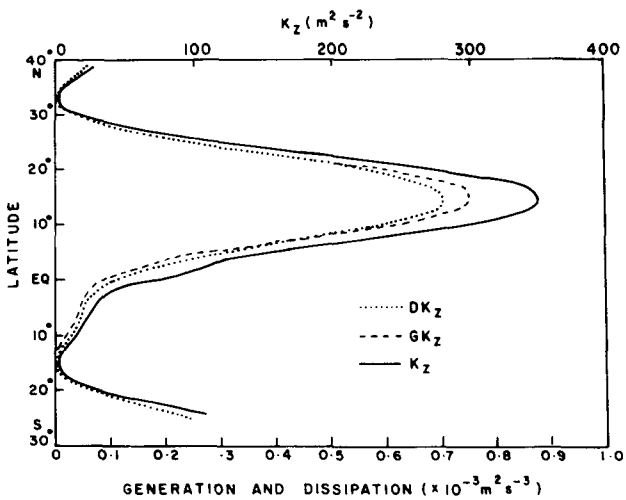

FIG. 14. Meridional profiles of zonal kinetic energy K_Z, generation GK_Z, and dissipation D_Z of zonal kinetic energy of the LIP case at day 120. Units for kinetic energy are meters squared per second squared, and energy generation and dissipation are in 10^{-3} m^2 s^{-1}.

linear unstable modes in its nonlinear evolution on the sphere. The nonlinear interactions further destabilize the initial easterly jet to a more unstable distribution during initial evolution. This effect is shown to be more pronounced for the random initial perturbation. The steady-state solution is characterized by dominating wave 6, which accounts for 98% of total eddy kinetic energy. The nonlinear evolution of perturbation can be understood in terms of zonal–wave and wave–wave interactions and its dissipation. The results obtained with the observed easterly jet do not exhibit expected complexities and are similar in many aspects to that obtained by the earlier workers for simple and idealized easterly jets (Kwon and Mak 1988; Feldstein 1991).

It is concluded that barotropic nonlinear interactions contribute positively towards the scale selection for the disturbances in the vicinity of the unstable easterly jet. The scale-selection mechanism due to nonlinear interactions is so strong that finally at steady state, a single wave is effectively present. The nonlinear interactions shift the preferred wave towards the longer wavelength. It has been found that nonlinear interactions modify the initial jet to a more asymmetric distribution of zonal wind around its center. It has been pointed out that this increase in degree of asymmetry of the jet is responsible for the further shift of nonlinear steady-state wave-amplitude maximum towards the equator. The steady-state wave shows some features such as maximum meridional velocity and average kinetic energy attained in the tropics, etc., which are very close to the observed values. It seems that the barotropic nonlinear process has no significant effect on the westward propagation speed of disturbance.

The correlation between latitudes of wave-amplitude maximum and meridional gradient of potential vorticity of zonal flow has been found to be stronger in this study than noticed for a linear unstable wave on the beta plane and on the sphere in the earlier studies. The correlation seems to be quite robust.

The use of a quasigeostrophic model in this study is justified through the following observations. Even close to the equator the irrotational wind is smaller than the nondivergent wind at 200 hPa during northern summer. This is valid for all synoptic-scale waves (Krishnamurti 1971). Further, Chen (1980) has computed stationary and transient components of zonal and eddy kinetic energy separately for the nondivergent and irrotational motion in the tropics (15°S–20°N) at 200 hPa during the summers of 1967 and 1972. His results show that the ratio of nondivergent kinetic energy to irrotational kinetic energy is about 4 even for transient eddy motion. The ratio is much higher for zonal and stationary motions. We have also computed the ratio in the tropical belt 14°S–14°N at 300-, 200-, and 100-hPa levels during July 1979 using FGGE IIIb reanalyzed data. We found the ratio for transient eddy motion nearly double at 100 hPa. Furthermore, we have also computed the zonal–wave and wave–wave interactions for the nondivergent and irrotational transient motion and noted that the nonlinear interaction for the former is one order more than the latter. It is not suggested here that the impact of irrotational motion on our results will be insignificant, but it will not of primary nature. It will be an interesting problem for future study to identify the role of irrotational motion in the nonlinear evolution of the tropical easterly jet by using a global primitive equation barotropic spectral model.

Acknowledgments. I wish to thank the Director of the Indian Institute of Tropical Meteorology for his encouragement and keen interest in the study. The author appreciates an anonymous reviewer for his comments and suggestions that led to a significant improvement in the presentation of the paper. The author is thankful to Smt. S. S. Desai and Shri D. W. Ganer for their help in preparation of the manuscript and diagrams. Finally, thanks go to Smt. S. S. Naik for typing the manuscript.

REFERENCES

Chen, T.-C., 1980: On the energy exchange between the divergent and rotational components of atmospheric flow over the tropics and subtropics at 200 mb during two northern summers. *Mon. Wea. Rev.*, **108**, 896–912.

——, and M.-C. Yen, 1991: Intraseasonal variations of the tropical easterly jet during the 1979 northern summer. *Tellus*, **43A**, 213–225.

Feldstein, S. B., 1991: A comparison of the weakly nonlinear instability and easterly jets in a two-layer beta-plane model. *J. Atmos. Sci.*, **48**, 1701–1717.

Krishnamurti, T. N., 1971: Observational study of the tropical upper tropospheric motion field during the Northern Hemisphere summer. *J. Appl. Meteor.*, **10**, 1066–1096.

——, S. M. Daggupaty, J. Fein, M. Kanamitsu, and J. D. Lee, 1973: Tibetan high- and upper-tropospheric tropical circulation during northern summer. *Bull. Amer. Meteor. Soc.*, **54**, 1234–1249.

Kwon, J. H., and M. Mak, 1988: On the equilibration in nonlinear barotropic instability. *J. Atmos. Sci.*, **45**, 294–308.

Mishra, S. K., 1987: Linear barotropic instability of the tropical easterly jet on a sphere. *J. Atmos. Sci.*, **44**, 373–383.

——, 1990: Barotropic spectral modelling of nonlinear interaction for transient waves in tropical easterly jet. *Mausam*, **41**, 241–250.

——, and P. S. Salvekar, 1980: Role of baroclinic instability in the development of monsoon disturbances. *J. Atmos. Sci.*, **37**, 383–394.

——, and M. K. Tandon, 1983: A combined barotropic–baroclinic instability study of the upper-tropospheric tropical easterly jet. *J. Atmos. Sci.*, **40**, 2708–2723.

——, D. Subrahmanyam, and M. K. Tandon, 1981: Divergent barotropic instability of the tropical asymmetric easterly jet. *J. Atmos. Sci.*, **38**, 2164–2171.

Robert, A. J., 1966: The integration of low order spectral form of the primitive meteorological equations. *J. Meteor. Soc. Japan*, **44**, 237–245.

Schoeberl, M. R., and R. S. Lindzen, 1984: A numerical simulation of barotropic instability. Part I: Wave–mean flow interaction. *J. Atmos. Sci.*, **41**, 1368–1379.

Shukla, J., 1977: Barotropic–baroclinic instability of mean zonal wind during summer monsoon. *Pure Appl. Geophys.*, **115**, 1449–1462.